Synthesis of Tin Catalyzed Silicon and Germanium Nanowires in a Solvent−Vapor System and Optimization of the Seed/Nanowire Interface for Dual Lithium Cycling

Synthesis of Tin Catalyzed Silicon and Germanium Nanowires in a Solvent−Vapor System and Optimization of the Seed/Nanowire Interface for Dual Lithium Cycling

Emma Mullane, Tadhg Kennedy, Hugh Geaney, Calum Dickinson, and Kevin M. Ryan*

Materials and Surface Science Institute and Department of Chemical and Environmental Sciences, University of Limerick, Limerick, Ireland

Ⓢ Supporting Information

ABSTRACT: Silicon and germanium nanowires are grown in high density directly from a tin layer evaporated on stainless steel. The nanowires are formed in low cost glassware apparatus using the vapor phase of a high boiling point organic solvent as the growth medium. HRTEM, DFSTEM, EELS, and EDX analysis show the NWs are single crystalline with predominant ⟨111⟩ growth directions. Investigation of the seed/nanowire interface shows that in the case of Si an amorphous carbon interlayer occurs that can be removed by modifying the growth conditions. Electrochemical data shows that both the tin metal catalyst and the semiconductor nanowire reversibly cycle with lithium when the interface between the crystalline phases of the metal and semiconductor is abrupt. The dually active nanowire arrays were shown to exhibit capacities greater than 1000 mAh g^{-1} after 50 charge/discharge cycles.

KEYWORDS: nanowire, silicon, germanium, tin catalyst, energy storage, lithium battery anodes
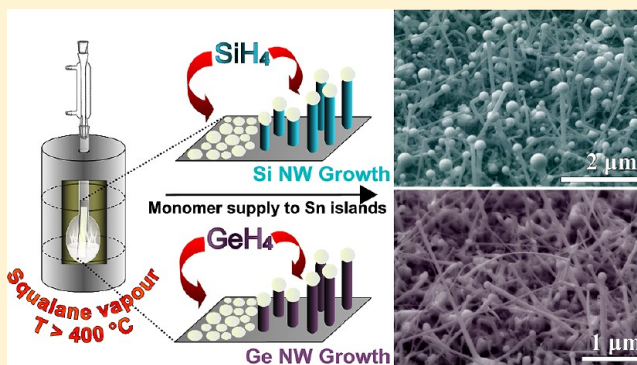
Si and Ge nanowires (NWs) have attracted intense research interest due to their suitability as building blocks for a range of devices in the semiconductor, photovoltaic, and energy storage industries.[1−3] The majority of the Si and Ge NW growth methods have focused on the use of Au as a catalyst material[4−6] due to its well established eutectic behavior with both Si and Ge.[4,5] In addition to its high cost and low abundance, Au has been found to be detrimental for electronic applications due to its propensity to act as an electron trap.[7,8] As a consequence, an extensive range of transition metals have been investigated as alternative catalysts with growth protocols largely dictated by whether the seed remains solid or liquid at the reaction temperature.[9−12] More recently, attention has turned to p-block metals with Bi,[13] Ga,[14] and In[15,16] showing promise for high purity NW formation. While the major focus of initial studies was directed toward nanoelectronics, the emergence of viable applications for Si and Ge NWs for storage (Li-ion batteries) and conversion (photovoltaics) places a different set of demands on the synthetic protocols. These bulk applications ideally require low cost routes with high-density NW formation occurring directly from substrates of interest using abundant and low cost precursors.[17−19] For example, as lithium battery anodes, NW diameter is of less significance, with Si or Ge NWs (up to 200 nm in diameter) showing resistance to pulverization during cycling allowing capacities of 3579 mAh g^{-1} (Si) and 1384 mAh g^{-1} (Ge) to be attained that are multiples of conventional materials (graphitic carbon 372 mAh

g^{-1}).[3,20−23] The choice of catalyst for this application is also relevant with Au not just of low abundance but also leading to irreversible capacity losses for the anode.[24,25] The catalyst material also adds to the weight of the anode thereby lowering the gravimetric capacity. The ideal catalyst would be of an abundant element that also cycles Li with Sn of particular interest given its high theoretical capacity (994 mAh g^{-1}) for Li uptake.[26] Sn catalyzed Si NWs have been formed using CVD[27] and supercritical fluid methods,[24] and while they have been investigated for use in Li storage applications, the Sn seed in these studies remained inactive for lithium cycling.[24]

We have recently developed a high boiling point solvent−vapor−growth (SVG) system as a low cost approach to high density NW growth. The method requires no addition of discrete nanoparticle seeds with NW growth occurring catalytically in the presence of a metal layer (Cu,[9,28,29] In[16]) by in situ formation of metal particles. The NWs grow by either a vapor−liquid−solid (VLS) or a vapor−solid−solid (VSS) protocol, depending on the boiling point of the metal, allowing very high yields of NWs to be attained at low temperature. Additionally as the NWs can be grown directly from a metal

layer, they are anchored to the metal surface, making them ideal for application as Li-ion battery anode materials.

Here we report the growth of high density Si and Ge NWs within the SVG system using Sn as the catalyst layer which is both elementally abundant and lithium active. The Sn catalyst layer is evaporated onto stainless steel (SS) substrates with growth occurring in high yield from the solvent−vapor system. The NWs are extensively examined by HRTEM, HRSEM, EELS, EDX, EBSD, and XRD analysis. For Si NWs, we show that the interface between the metal tip and the NW is tunable occurring either as an amorphous region (<10 nm) or atomically abrupt according to the growth conditions. The presence of the amorphous layer prevented Li cycling for the Sn. However, the atomically abrupt metal-semiconductor NWs allowed dual cycling where both the metal and the semiconductor were active as anode materials. This approach allows for significant advances in NW battery development, combining a low cost solution based approach with an abundant catalyst material that contributes to the device efficiency.

■ RESULTS AND DISCUSSION

The SVG system, Figure 1, uses a long-necked round-bottomed flask within a three zone furnace, allowing thermally localizable
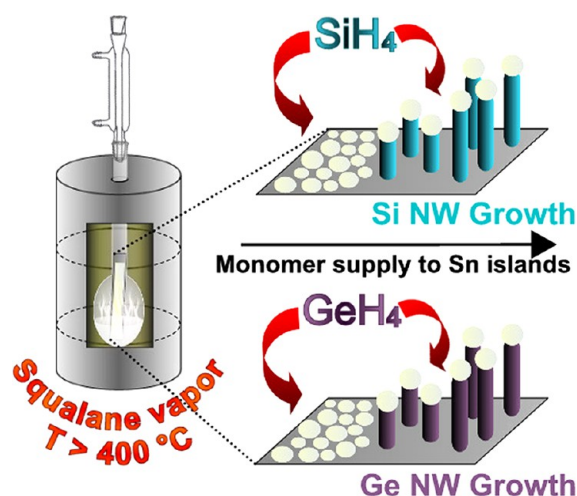

Figure 1. Schematic illustrating the solvent−vapor−growth system used.

NW growth on the substrate incorporated within the vapor region of the high boiling point solvent squalane. Si and Ge NW growth reactions were carried out using a 20 nm thick thermally evaporated catalytic Sn layer on SS substrates. Due to its low melting point, Sn formed discrete islands at the reaction temperatures examined (>400 °C) that nucleate NWs via the VLS mechanism (Sn melting point, 231.9 °C). This Sn island formation circumvented the need for the addition of discrete catalyst seeds allowing the growth of highly dense Si or Ge NWs directly from the underlying growth substrate.

Si NW Growth. Due to the high decomposition temperature of the phenylsilane (PS) precursor, reaction temperatures of 460 °C (for 1 h) were required for Si NW growth. Phenylsilane undergoes phenyl redistribution at elevated temperatures to supply the monomer for NW growth.[30] A high magnification SEM image (taken at a 50° tilt) showing an example of Sn catalyzed Si NWs (105 ± 30 nm) grown on SS is shown in Figure 2a. The high density of Si NWs grown on the
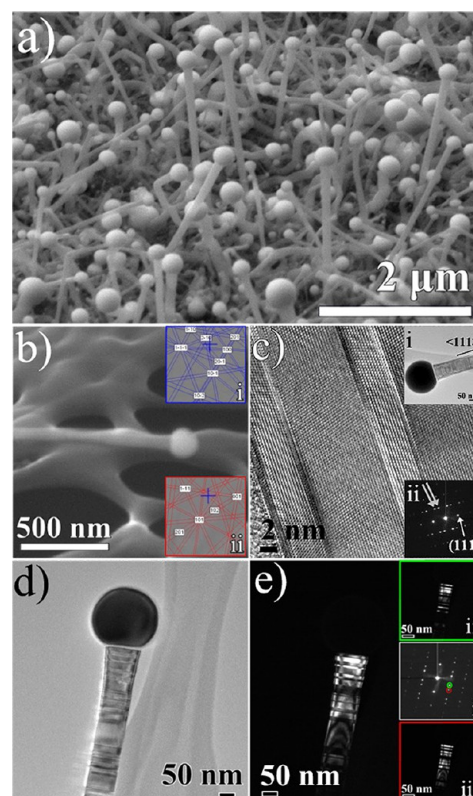

Figure 2. Analysis of Sn catalyzed Si NWs grown on SS. (a) High magnification 50° tilted SEM image showing the typical morphology and diameter distribution of the NWs. The NWs can be seen to be growing from and are connected to the underlying substrate. (b) Point EBSD analysis of the NWs formed with corresponding patterns indexed for tetragonal Sn (i) and cubic Si (ii) for the seed and NW, respectively. (c) High resolution TEM image of corresponding Sn catalyzed Si NW in inset (i) showing twin defects along the length of the NW with inset SAED pattern (ii) (twinned spots highlighted by gray arrows). (d) Low magnification TEM image of Sn seeded Si NW. (e) DF-TEM analysis of NW in (d) with SAED of Si segment in (i) and DF-TEM images highlighting defects associated with each of a pair of twinned spots highlighted in green (ii) and red (iii), respectively. The main image is a composite of insets ii and iii.

substrate can clearly be seen with NW growth extending over all the substrate that was localized within the vapor phase of the system (Supporting Information, Figure S1). The Sn catalyst particles can be seen as bright spots due to their higher Z contrast in comparison to Si.

For EBSD, NWs were sonicated from the SS substrate before being dropcast on a TEM grid. Point analysis of a typical NW and seed (Figure 2b) gave EBSD patterns consistent with tetragonal Sn with space group $I41/amd$ (Figure 2b, inset i) and diamond cubic Si with space group $Fd\bar{3}m$ (Figure 2b, inset ii), respectively (an additional NW examined analyzed using EBSD can be seen in Supporting Information, Figure S2). The low resolution image in Figure 2c (inset i) shows the clear contrast and diameter difference between the Sn catalyst and Si NW (ratio typically ≈2.25:1 for seed/NW diameter). The SAED pattern in Figure 2c (inset ii) gives spots that are consistent with the twin defected Si NW and a (111) spot indicative of a ⟨111⟩ growth direction. These {111} oriented twin defects were found to be perpendicular to the NW growth direction in all cases. A lattice resolved image of the Si NW taken close to the NW/seed interface further highlights the
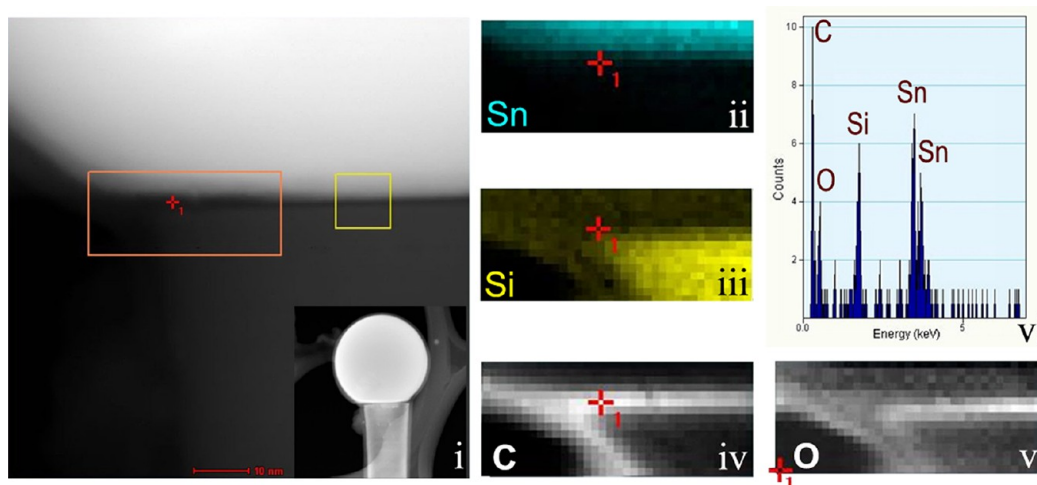
Figure 3. DFSTEM image of Sn seeded Si NW taken from the inset NW in i. EDX elemental maps for Sn (ii) and Si (iii) within the region highlighted in the orange rectangle are shown along with corresponding EELS maps for C (iv) and O (v). Inset vi is an overall EDX spectrum of the region.

presence of twin defects (Figure 2c). Similar types of transverse twin faults have previously been noted for Si NWs grown from comparable low melting point metals (In[15] and Ga[31]). It can also be seen that the area closest to the Sn catalyst is amorphous (due to the abrupt termination of crystalline fringes in the image) (Supporting Information, Figure S3). The composition of this interfacial region was analyzed using EELS and EDX analysis and will be discussed later in the text. This interface is quite different to those typically noted for the archetypal VLS NW catalyst Au, which characteristically possess a hemispherical catalyst tip in contact with the extruded NW.[7] It is likely that the nature of Sn as a "type B" catalyst (which forms a eutectic alloy that is composed of <1% Si)[32] coupled with the low melting point and low surface tension of Sn[33] is a key factor in determining this interfacial behavior as other type B catalysts have been found to possess atypical catalyst/NW interfaces.[15,16,32,34]

Figure 2d is a low magnification TEM image of a Sn seeded Si NW with twin defects along its length. DF-TEM analysis (Figure 2e) of the same NW was used to highlight the defects associated with a pair of twinned SAED spots, Figure 2e (inset i). By centering the objective aperture over the SAED spot highlighted in green, Figure 2e (inset i), the band of defects associated with this spot are revealed (Figure 2e, inset ii). The remaining set of defects was imaged when the procedure was repeated for the SAED twin spot highlighted in red (Figure 2e, inset iii). An overlaid DF-TEM image is presented in the main image of Figure 2e.

Additional NW/seed interfaces were analyzed using TEM to investigate if all the NWs in the sample possessed an amorphous region between the crystalline seed and NW (Supporting Information Figure S4). It must be noted that the NWs were tilted to a major zone axis in each case to clearly identify the interface. The DFSTEM image shown in Figure 3 (main and inset i) shows the amorphous region previously noted. The seed is similarly spherical to that seen in Figure 2 with a flat edge in line with the resultant Si NW. EDX elemental maps and EELS maps were taken for the region highlighted in orange (Figure 3, main). The EDX maps for Sn and Si are shown in insets ii and iii corresponding to the catalyst seed and NW, respectively. For the EELS maps, C can be seen to be the major constituent of the region between the

Sn catalyst and Si NW. The presence of O was noted primarily next to the Si NW, which is consistent with the $SiO_{x(x\leq2)}$ oxide covering typically noted for Si NWs exposed to ambient conditions.[16] This amorphous region was found to be present for Sn catalyzed Si NWs regardless of reaction time, temperature, and NW diameter. The source of amorphous C noted in the growth system is likely due to partial decomposition of the organic solvent squalane at the elevated temperatures. However, we do not believe that the C is purely localized at this seed/NW interface, that it is during NW growth or postgrowth that C coats the Sn seeded Si NWs, and that the subsequent cooling and dewetting of the seed at the growth interface postreaction expose this C region. As the NW catalyst was obviously attached to the NW during growth, this exposed amorphous region between the NW and the catalyst may thus be due to a dewetting effect caused by slow cooling employed in the growth system coupled with the atypical wetting behavior of Sn as a low surface tension metal seed.[33,35] By fast quenching the system above the melting temperature of the Sn seed, rapid solidification of the catalytic droplet takes place at the growth front and leads to the absence of an amorphous interfacial region. To verify this, the role of NW growth termination was investigated by rapidly quenching the NW growth reaction above the melting point of the Sn.

Figure 4 shows TEM analysis of a NW taken from a quenched reaction. The HRTEM image in Figure 4a taken of the NW in Figure 4 (inset i) shows an example of the Si NW/Sn catalyst interface with no visible gap between the catalyst and NW. The corresponding FFT pattern for the Si NW, Figure 4 (inset ii), is consistent with diamond cubic Si with a ⟨111⟩ growth direction. The annular DF-STEM image in Figure 4b taken from the same NW (on the same major zone axis) and overlaid EDX line profile indicate the presence of nonzero Si and Sn at the catalyst/NW interface in contrast to that seen in Figure 3c, suggesting that there is no gap between the NW and the catalyst. This is consistent with all the NWs formed using the rapid quenching approach (see Supporting Information, Figure S5 for additional examples).

Ge NW Growth. Ge NWs were grown from the evaporated Sn layer at the lower reaction temperature of 430 °C due to the lower thermal stability of diphenylgermane (DPG) in comparison to PS with a typical reaction time of 10 min.
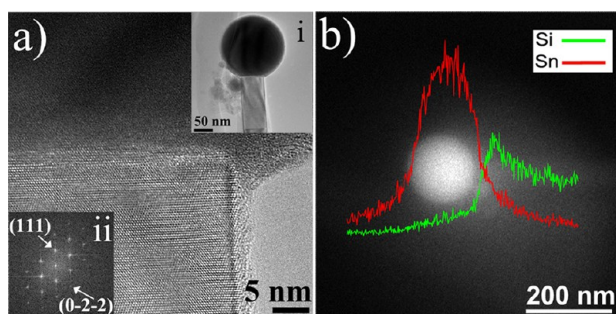
Figure 4. TEM analysis taken from a quenched Sn catalyzed Si NW. (a) HRTEM image of Sn/Si interface with corresponding low magnification image inset (i) and corresponding FFT of Si NW segment inset (ii). (b) DF-STEM image of NW from (a) and overlaid EDX line profile analysis.

Uniform high density NW formation was again noted across the substrates (typically ≈10 cm²) which had a visibly altered, characteristic purple color when compared to the pre-reaction gray color (Supporting Information, Figure S6). The NWs were seen to be attached to the underlying SS with a mean diameter of 70 ± 18 nm (Figure 5a).

TEM analysis of the Sn catalyzed Ge NWs is shown in Figure 5b. In comparison to the spherical seeds noted for the Si NWs
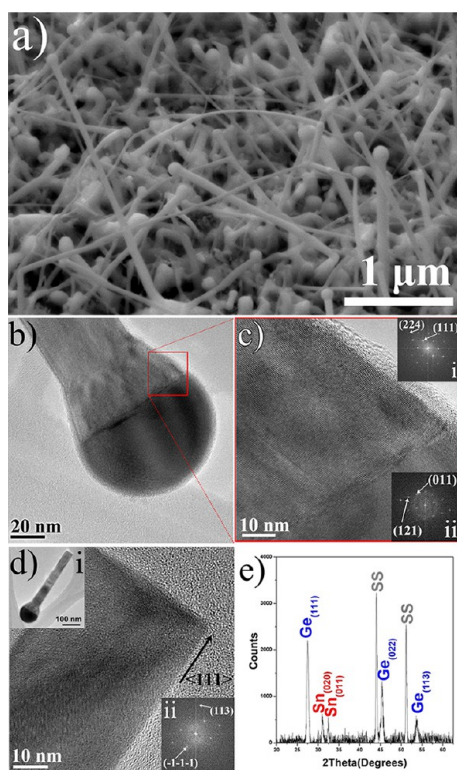

Figure 5. Analysis of Sn seeded Ge NWs grown on SS. (a) Tilted high magnification SEM image showing the high density, high aspect ratio NWs growing from the underlying substrate. The pseudospherical catalyst tips can clearly be seen in the image. (b) TEM image of Ge NW with Sn catalyst tip and tapered Ge region between the main Ge NW section and Sn catalyst. (c) High resolution image of tapered Ge region attached to the Sn catalyst in (b) with inset FFTs indexed for (i) diamond cubic Ge and (ii) tetragonal Sn. (d) Flat end of the NW shown in inset (i) with inset FFT (ii) indexed for cubic Ge. (e) XRD of Sn catalyzed Ge NWs on SS.

grown from Sn previously, the Ge/Sn interface was noticeably different with a far more hemispherical catalyst shape and an average seed/NW diameter ratio of ≈1.75:1. The contrast difference between the catalyst and NW was also less pronounced given the closer Z number relationship between Sn and Ge. Additionally, the 20−40 nm region of the NW closest to the Sn catalyst was noticeably larger in diameter than the remaining NW portion (see additional example in Supporting Information, Figure S7). The lattice resolved TEM image in Figure 5c shows the interface between the Sn catalyst and the tapered portion of the Ge NW in Figure 5b (The tapering can be controlled by modifying the reaction conditions; see discussion, Supporting Information S8). The NW can be seen to be covered in an amorphous oxide coating which is consistent to that previously noted for Ge NWs synthesized using the SVG system.[9] The FFT (Figure 5c, inset i) is indexed with spots that correspond to the those expected for diamond cubic Ge and are consistent with a ⟨111⟩ growth direction for the NW. The FFT for the Sn catalyst, Figure 5c (inset ii), is indexed with spots which correspond to tetragonal Sn as expected. The high resolution image shown in Figure 5d was taken from the end of the NW shown in Figure 5d, inset i, and exhibits a consistent ⟨111⟩ growth direction throughout (elucidated from FFT in Figure 5d, inset ii). XRD analysis of the as-synthesized material gave reflections consistent with cubic Ge (space group $Fd\bar{3}m$) and tetragonal Sn (space group $I41/amd$) with remaining peaks corresponding to the underlying SS.

In situ observations would be ideal to understand the behavior of a low surface tension metal seed during Si and Ge NW growth and postgrowth in the SVG system used here. A common observation of the typical VLS growth model (e.g., Au seeded Si) has been that in the absence of external perturbations, the liquid droplet rests on the {111} growth front without touching the lateral surface of the NW with the contact angle remaining unchanged during the growth process.[36] Two factors influencing the Si growth system mean these assumptions cannot hold true. The first relates to the instability of Sn as a catalytic droplet. A recent study by Yu et al. highlighted the instability of Sn as a seed for Si NW growth owing to its low surface tension and found that ultrathin sidewall-spreading of the catalyst layer helped stabilize the low surface tension Sn seed during the growth process.[33] The second issue has to do with the large concentration of lamellar {111} twins that bisect the Si NWs perpendicular to the growth direction which gives rise to a bamboo-like appearance. Twin formation in VLS grown Si and Ge NWs is a common feature and has been noted in numerous studies in recent years.[37−39] The {111} twin energies of Si and Ge are of the order of the thermal energy of the system, and when comparing Ge NWs and Si NWs in the SVG system used here, the higher reaction temperature required for Si NW growth (450 °C) compared to Ge NW growth (420 °C) may explain the prevalence of twin defects in Si NWs. A report by Davidson et al. showed that {111} twin formation causes the restructuring of the NW sidewall facet which causes variations in the growth angle that must be accommodated by the catalyst droplet in order to facilitate NW growth.[40] The instability of Sn as a low surface tension metal catalyst along with the presence of twin defects in Si NWs at elevated temperatures could contribute to an atypical seed/NW growth interface for the Si NWs in this study.

Electrochemical data was used to invesigate the importance of optimizing the NW/catalyst interface to ensure that both

materials were Li active. Differential capacity plots (Figure 6) were obtained from galvanostatic charging and discharging at a
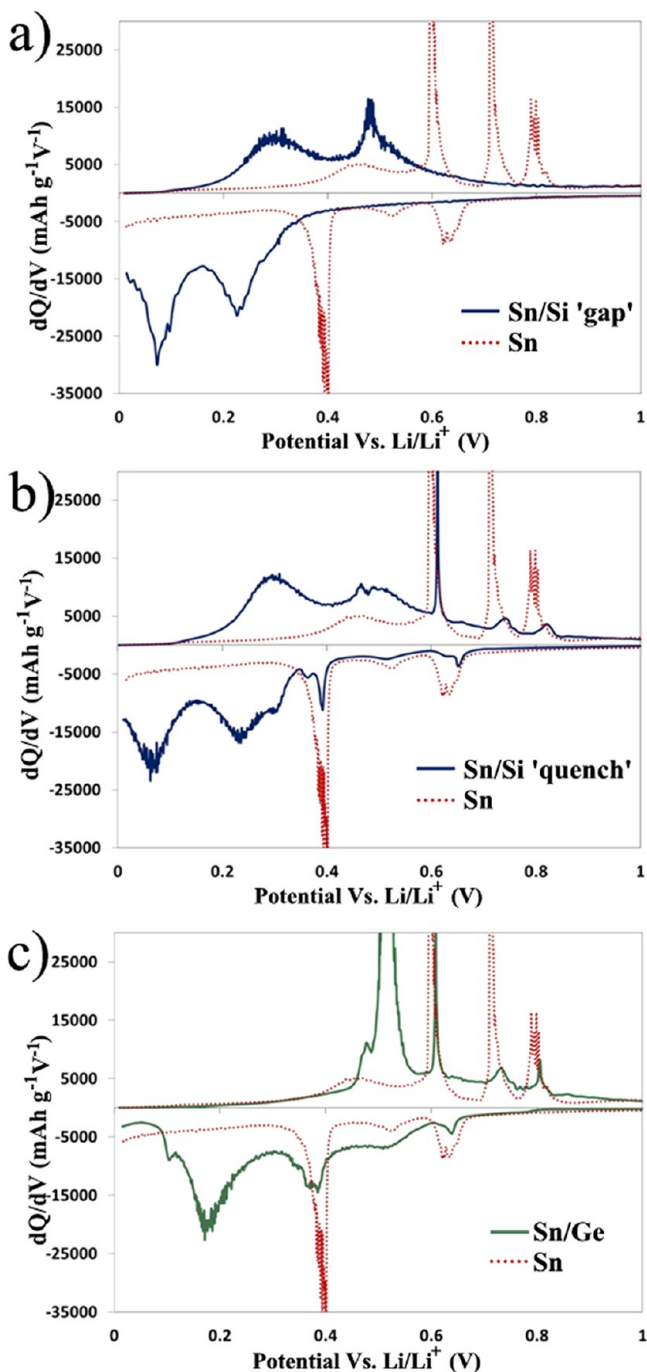

Figure 6. Differential capacity plots of (a) Sn catalyzed Si NWs with ≈10 nm "gap" at Sn/Si interface after second cycle, (b) Sn catalyzed Si NWs that underwent a rapid quench to eliminate "gap" after 10 cycles, and (c) Sn catalyzed Ge after 10 cycles.

$C/2$ rate (Supporting Information, Figure S9) of samples (a) Si NWs with an amorphous gap between the Si and Sn, (b) Si NWs with no amorphous layer, and (c) Sn seeded Ge NWs. The use of differential capacity plots in this case allows for clear identification of peaks that correspond to lithium alloying/dealloying of both the metal seed and semiconductor NW. In all cases the dotted line represents a control sample which highlights the characteristic charge and discharge peaks for a 20

nm thick Sn layer on SS. The cathodic branch has three peaks at 0.63, 0.53, and 0.39 V attributed to the alloying of Li with Sn, where each individual peak is a result of the formation of a different Li_xSn phase.[41,42] Conversely, the four peaks in the anodic branch at 0.46 V, 0.60 V, 0.73 V, and 0.80 V are due to the dealloying reaction. The data obtained for Sn catalyzed Si NWs that contain an amorphous gap are presented in Figure 6a. The Sn seeded Si NW electrode was cycled at a current density of 1245 mA/g (C/2 rate). The solid line has two well-defined peaks on both the charge (at approximately 0.23 and 0.09 V) and discharge (approximately 0.3 and 0.5 V) sections which are characteristic of the phase changes associated with the lithiation and delithiation of cubic Si.[3,43−45] It can be seen that there are no peaks associated with the alloying/dealloying of Sn catalyst seeds, confirming that they are not active in this configuration. The absence of Sn peaks indicates that no electrical contact exists between the catalyst and the current collector and thus there is no electrochemical driving force for the reaction to occur. This is logical given the relatively large size (≈10 nm) amorphous "gap" between the NW and the Sn catalyst. In this case the interface between the NW and seed is not strong enough to accommodate the expansion caused by Li insertion and thus the Sn catalysts become detached from the NWs and cannot cycle. This data was obtained from the second charge/discharge cycle where already no Sn signal associated with lithiation/delithiation was present. Similar inactive electrochemical characteristics existed when the Si nanowires possessing an amorphous gap were scanned at a slower scan rate of C/5 (Supporting Information, Figure S10).

In contrast, the plot shown in Figure 6b demonstrates differential capacity data obtained from the 10th charge/discharge cycle for quenched Sn catalyzed Si NWs (i.e., without the amorphous gap). It can be seen in the plot that the characteristic Si alloying/dealloying peaks noted in Figure 6a persist and that additional peaks that match well with the Sn reference data are present. The data was taken after 10 cycles to emphasize that the Sn is well adhered to the Si NWs and is Li active over extended cycles. This is a good indication that the quench step is a prerequiste for the formation of Si NWs from Sn where both the seed and NW are Li active.

Electrochemical data obtained for the Ge NWs was found to be independent of the preparation method (i.e., NWs with and without the tapered section performed identically). In Figure 6c differential capacity data is presented for Sn catalyzed Ge NWs which was again obtained from the 10th charge/discharge cycle. The main Ge peaks are located at 0.18 and 0.11 V for the charge and 0.48 and 0.51 V for the discharge and are consistent with those previously noted for the phase changes associated with Ge lithiation/delithiation.[46−49] The additional peaks noted in the plot are consistent with the presence of Sn as a Li active material and are evidence of the fact that the Sn catalyst seeds remain on the NWs over extended cycles.

Extended galvanostatic charge/discharge experiments were performed on the rapidly quenched Sn catalyzed Si NWs (Figure 7a) and Sn catalyzed Ge NWs (Figure 7b) at a rate of $C/2$ (1245 mA/g for Sn seeded Si and 640 mA/g for Sn seeded Ge) for 50 cycles. Crucially, in both cases the weights of the entire Li-active anode material (NW masses and catalyst masses) were taken into account when calculating the capacity figures for the plots shown (see Supporting Information for values used to determine C). The Si/Sn composite material shows a capacity of 1078 mAh g^{-1} after 50 cycles with the capacity for the Sn/Ge composite analogue at 1000 mAh g^{-1}
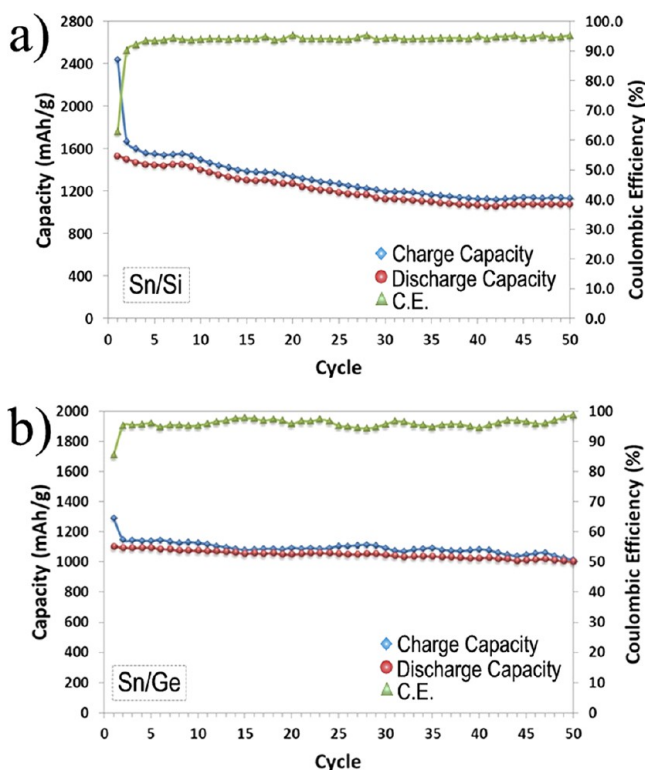
Figure 7. Plot of charge/discharge capacities and Coulombic efficiencies for (a) Sn seeded Si NWs with no amorphous interfacial Sn/Si region and (b) Sn seeded Ge NWs.

after the same number of cycles. The NWs grown using the SVG system show average Coulombic efficiencies of 94.2% for the dually active Sn/Si anode material and 96.06% for its Ge counterpart.

CONCLUSION

In conclusion, we have presented a low-cost glassware based protocol for the growth of Sn catalyzed Si and Ge NWs directly on SS current collector substrates. The method does not require the addition of discrete catalyst particles but relies on their in situ formation by annealing of an evaporated Sn layer on stainless steel. The single crystal NWs grow in high density and exhibit predominantly ⟨111⟩ growth directions. The nature of the catalyst/NW interface was analyzed and controlled by varying key synthetic parameters. Differential capacity plots highlighted the dual lithium cycling of both the Sn seed and the group IV NWs when the interface is optimized. In addition to its high elemental abundance, the ability of the catalyst itself to cycle lithium allows for the contribution of both seed and NW toward more efficient and cost-effective Li-ion battery anode materials. The Sn/Si and Sn/Ge NWs show excellent capacities of 1078 mAh g^{-1} and 1000 mAh g^{-1}, respectively (after 50 charge/discharge cycles) calculated using the combined mass of the NW and Li-active catalyst material.

METHODS

Substrate Preparation and Postsynthetic Treatment. Sn substrates were prepared by evaporating 99.99% Sn (Kurt J Lesker company) in a glovebox based evaporation unit. Optimal growth was achieved for Sn thicknesses of between 20 and 30 nm. The substrates were stored in an Ar glovebox prior to reactions, and contact with O$_2$ was minimized. After synthesis, the substrates were simply rinsed with

toluene, to remove excess solvent, and dried using a nitrogen line. No additional cleaning steps were required.

Reaction Setup. Reactions were carried out in custom-made Pyrex round-bottomed flasks. The growth substrates were placed vertically in the flask which was attached to a Schlenk line setup via a water condenser. Seven milliliters of squalane (Aldrich 99%) was added, and the system was then ramped to a temperature of 125 °C using a three-zone furnace. A vacuum of at least 100 mTorr was applied for 1 h to remove moisture from the system. Following this, the system was purged with Ar. The flask was then ramped to the reaction temperature under a constant Ar flow.

For Si, reactions were always conducted above 450 °C (typically 460 °C). This was due to the use of the PS precursor which was found not to decompose below this temperature. Ge reactions were carried out at 430 °C. A water condenser was used to control the solvent reflux and ensure that the reaction was kept under control. At the correct reaction temperature, PS (97% Aldrich) or DPG (97% Gelest Inc.) was injected through a septum cap into the system. Various reaction times were investigated. To terminate the reaction, the furnace was opened, and the setup was allowed to cool to room temperature before extracting the NW coated substrates.

Analysis. Scanning electron microscopy (SEM) analysis was performed on a Hitachi SU-70 system operating between 3 and 20 kV. The Sn substrates were untreated prior to SEM analysis. For transmission electron microscopy (TEM) analysis, the NWs were removed from the growth substrates through the use of a sonic bath. TEM analysis was conducted using a 200 kV JEOL JEM-2100F field emission microscope equipped with a Gatan Ultrascan CCD camera and EDAX Genesis EDS detector. Electron dispersive X-ray (EDX) spectroscopy of the NWs was conducted on Au TEM grids. Electron energy loss spectroscopy (EELS) was performed on a FEI Titan field emission TEM with accelerating voltages between 80 kV and 300 kV. X-ray diffraction (XRD) analysis was conducted using a PANalytical X'Pert PRO MRD instrument with a Cu Kα radiation source (λ = 1.5418 Å) and an X'celerator detector. Electron backscatter diffraction (EBSD) was carried out at 20 kV and beam current 1.54 nA using an Oxford Instruments Nordlys EBSD detector and HKL Channel 5 software.

Electrochemical Measurements. The electrochemical performance was evaluated by assembling two electrode Swagelok type cells in an Ar filled glovebox. The cells consisted of Sn seeded Si or Ge NWs or a blank 20 nm evaporated layer of Sn on SS substrates as the working electrode, Li foil as the counter and reference electrode, a porous polyethene separator, and an electrolyte solution of 1 M LiPF$_6$ in ethylene carbonate/dimethyl carbonate (EC/DMC) (1:1 v/v). The measurements were carried out galvanostatically using an Autolab PGSTAT100 at a C/2 rate in the potential range of 0.01−1.5 V versus Li/Li$^+$.

ASSOCIATED CONTENT

Ⓢ Supporting Information

SEM, TEM, EDS, and EBSD analysis of Sn catalyzed Si NWs. SEM and HRTEM images of Sn catalyzed Ge NWs, photographic image of centimeter scale substrates pre- and postsynthesis. Voltage profiles of Sn seeded Si and Ge NWs. Additional electrochemical data including differential capacity plots for Sn seeded Si at a slower charge/discharge rate and values used to calculate C. This material is available free of charge via the Internet at http://pubs.acs.org.

AUTHOR INFORMATION

Corresponding Author

*E-mail: kevin.m.ryan@ul.ie.

Notes

The authors declare no competing financial interest.

ACKNOWLEDGMENTS

REFERENCES

(1) Cui, Y.; Zhong, Z.; Wang, D.; Wang, W. U.; Lieber, C. M. *Nano Lett.* **2003**, *3*, 149.

(2) Garnett, E.; Yang, P. *Nano Lett.* **2010**, *10*, 1082.

(3) Chan, C. K.; Peng, H.; Liu, G.; McIlwrath, K.; Zhang, X. F.; Huggins, R. A.; Cui, Y. *Nat. Nanotechnol.* **2008**, *3*, 31.

(4) Hanrath, T.; Korgel, B. A. *J. Am. Chem. Soc.* **2002**, *124*, 1424.

(5) Lu, X.; Hanrath, T.; Johnston, K. P.; Korgel, B. A. *Nano Lett.* **2002**, *3*, 93.

(6) Holmes, J. D.; Johnston, K. P.; Doty, R. C.; Korgel, B. A. *Science* **2000**, *287*, 1471.

(7) Hannon, J. B.; Kodambaka, S.; Ross, F. M.; Tromp, R. M. *Nature* **2006**, *440*, 69.

(8) Allen, J. E.; Hemesath, E. R.; Perea, D. E.; Lensch-Falk, J. L.; LiZ., Y.; Yin, F.; Gass, M. H.; Wang, P.; Bleloch, A. L.; Palmer, R. E.; Lauhon, L. J. *Nat. Nanotechnol.* **2008**, *3*, 168.

(9) Geaney, H.; Dickinson, C.; Barrett, C. A.; Ryan, K. M. *Chem. Mater.* **2011**, *23*, 4838.

(10) Kodambaka, S.; Tersoff, J.; Reuter, M. C.; Ross, F. M. *Science* **2007**, *316*, 729.

(11) Tuan, H.-Y.; Lee, D. C.; Korgel, B. A. *Angew. Chem.* **2006**, *118*, 5308.

(12) Kamins, T. I.; Williams, R. S.; Basile, D. P.; Hesjedal, T.; Harris, J. S. *J. Appl. Phys.* **2001**, *89*, 1008.

(13) Heitsch, A. T.; Fanfair, D. D.; Tuan, H.-Y.; Korgel, B. A. *J. Am. Chem. Soc.* **2008**, *130*, 5436.

(14) Pan, Z.; Dai, S.; Beach, D. B.; Lowndes, D. H. *Nano Lett.* **2003**, *3*, 1279.

(15) Wang, Z. W.; Li, Z. Y. *Nano Lett.* **2009**, *9*, 1467.

(16) Geaney, H.; Kennedy, T.; Dickinson, C.; Mullane, E.; Singh, A.; Laffir, F.; Ryan, K. M. *Chem. Mater.* **2012**, *24*, 2204.

(17) Yuan, F.-W.; Yang, H.-J.; Tuan, H.-Y. *J. Mater. Chem.* **2011**, *21*, 13793.

(18) Yang, H.-J.; Tuan, H.-Y. *J. Mater. Chem.* **2012**, *22*, 2215.

(19) Barrett, C. A.; Gunning, R. D.; Hantschel, T.; Arstila, K.; O'Sullivan, C.; Geaney, H.; Ryan, K. M. *J. Mater. Chem.* **2010**, *20*, 135.

(20) Chan, C. K.; Zhang, X. F.; Cui, Y. *Nano Lett.* **2007**, *8*, 307.

(21) Chockla, A. M.; Harris, J. T.; Akhavan, V. A.; Bogart, T. D.; Holmberg, V. C.; Steinhagen, C.; Mullins, C. B.; Stevenson, K. J.; Korgel, B. A. *J. Am. Chem. Soc.* **2011**, *133*, 20914.

(22) Chan, C. K.; Patel, R. N.; O'Connell, M. J.; Korgel, B. A.; Cui, Y. *ACS Nano* **2010**, *4*, 1443.

(23) Yuan, F.-W.; Yang, H.-J.; Tuan, H.-Y. *ACS Nano* **2012**, *6*, 9932.

(24) Chockla, A. M.; Klavetter, K.; Mullins, C. B.; Korgel, B. A. *Chem. Mater.* **2012**, *24*, 3738.

(25) Chockla, A. M.; Bogart, T. D.; Hessel, C. M.; Klavetter, K. C.; Mullins, C. B.; Korgel, B. A. *J. Phys. Chem. C* **2012**, *116*, 18079.

(26) Hassoun, J.; Panero, S.; Reale, P.; Scrosati, B. *Int. J. Electrochem. Sci.* **2006**, *1*, 110.

(27) Rathi, S. J.; Jariwala, B. N.; Beach, J. D.; Stradins, P.; Taylor, P. C.; Weng, X.; Ke, Y.; Redwing, J. M.; Agarwal, S.; Collins, R. T. *J. Phys. Chem. C* **2011**, *115*, 3833.

(28) Mullane, E.; Geaney, H.; Ryan, K. M. *Chem. Commun.* **2012**, *48*, 5446.

(29) Geaney, H.; Dickinson, C.; O'Dwyer, C.; Mullane, E.; Singh, A.; Ryan, K. M. *Chem. Mater.* **2012**, *24*, 4319.

(30) Tuan, H.-Y.; Korgel, B. A. *Chem. Mater.* **2008**, *20*, 1239.

(31) Conesa-Boj, S.; Zardo, I.; Estrade, S.; Wei, L.; Alet, P. J.; Cabarrocas, P. R. I; Morante, J. R.; Peiro, F.; Morral, A. F. I; Arbiol, J. *Cryst. Growth Des.* **2010**, *10*, 1534.

(32) Schmidt, V.; Wittemann, J. V.; Gosele, U. *Chem. Rev.* **2010**, *110*, 361.

(33) Yu, L.; Fortuna, F.; O'Donnell, B.; Patriache, G.; Cabarrocas, P. R. i. *Appl. Phys. Lett.* **2011**, *98*, 123113.

(34) Sharma, S.; Sunkara, M. K. *Nanotechnology* **2004**, *15*, 130.

(35) Dubrovskii, V. G.; Cirlin, G. E.; Sibirev, N. V.; Jabeen, F.; Harmand, J. C.; Werner, P. *Nano Lett.* **2011**, *11*, 1247.

(36) Ross, F. M. *Rep. Prog. Phys.* **2010**, *73*, 114501.

(37) Hanrath, T.; Korgel, B. A. *Small* **2005**, *1*, 717.

(38) Carim, A. H.; Lew, K. K.; Redwing, J. M. *Adv. Mater.* **2001**, *13*, 1489.

(39) Tang, Q.; Liu, X.; Kamins, T. I.; Solomon, G. S.; Harris, J. S. *Appl. Phys. Lett.* **2002**, *81*, 2451.

(40) Davidson, F. M.; Lee, D. C.; Fanfair, D. D.; Korgel, B. A. *J. Phys. Chem. C* **2007**, *111*, 2929.

(41) Luo, B.; Wang, B.; Li, X.; Jia, Y.; Liang, M.; Zhi, L. *Adv. Mater.* **2012**, *24*, 3538.

(42) Wang, G.; Ma, Y. Q.; Liu, Z. Y.; Wu, J. N. *Electrochim. Acta* **2012**, *65*, 275.

(43) Liu, W.; Wang, J.; Wu, H.; Shieh, D.; Yang, M.; Wu, N. *J. Electrochem. Soc.* **2005**, *152*, A1719.

(44) Ng, S. H.; Wang, J.; Wexler, D.; Konstantinov, K.; Guo, Z. P.; Liu, H. K. *Angew. Chem., Int. Ed.* **2006**, *45*, 6896.

(45) Wang, W.; Kumta, P. N. *ACS Nano* **2010**, *4*, 2233.

(46) Seo, M. H.; Park, M.; Lee, K. T.; Kim, K.; Kim, J.; Cho, J. *Energy Environ. Sci.* **2011**, *4*, 425.

(47) Rudawski, N.; Darby, B.; Yates, B.; Jones, K.; Elliman, R.; Volinsky, A. *Appl. Phys. Lett.* **2012**, *100*, 83111.

(48) Laforge, B.; Levan-Jodin, L.; Salot, R.; Billard, A. *J. Electrochem. Soc.* **2008**, *155*, A181.

(49) Graetz, J.; Ahn, C.; Yazami, R.; Fultz, B. *J. Electrochem. Soc.* **2004**, *151*, A698.